



Design and Construction of Three-Dimensional Physiologically-Based Vascular Branching Networks for Respiratory Assist Devices

Journal:	<i>Lab on a Chip</i>
Manuscript ID	LC-ART-04-2021-000287.R2
Article Type:	Paper
Date Submitted by the Author:	26-Sep-2021
Complete List of Authors:	<p>Santos, Jose; Charles Stark Draper Laboratory Inc, Division of Bioengineering Gimbel, Alla; Charles Stark Draper Laboratory Inc, Division of Bioengineering Peppas, Athanasios; Cardiovascular Research Foundation Truslow, James; Charles Stark Draper Laboratory Inc, Division of Bioengineering Lang, Daniel; Charles Stark Draper Laboratory Inc, Mechanical Engineering Division Sukavaneshvar, Sivaprasad; Thrombodyne Inc., Solt, Derek; Thrombodyne Inc. Mulhern, Thomas; Charles Stark Draper Laboratory Inc, Division of Bioengineering Markoski, Alex; Charles Stark Draper Laboratory Inc, Division of Bioengineering Kim, Ernest; Charles Stark Draper Laboratory Inc, Division of Bioengineering Hsiao, James; Charles Stark Draper Laboratory Inc, Division of Bioengineering Lewis, Diana; Charles Stark Draper Laboratory Inc, Division of Bioengineering Harjes, Daniel; Charles Stark Draper Laboratory Inc, Mechanical Engineering Division DiBiasio, Christopher; Charles Stark Draper Laboratory Inc, Mechanical Engineering Division Charest, Joseph; Charles Stark Draper Laboratory Inc, Division of Bioengineering Borenstein, Jeffrey; Charles Stark Draper Laboratory Inc, Division of Bioengineering</p>

ARTICLE

Design and Construction of Three-Dimensional Physiologically-Based Vascular Branching Networks for Respiratory Assist Devices

Jose A. Santos,^{*a} Alla A. Gimbel,^{*a} Athanasios Peppas,^b James G. Truslow,^{†a} Daniel A. Lang,^a Sivaprasad Sukavaneshvar,^c Derek Solt,^c Thomas J. Mulhern,^a Alex Markoski,^a Ernest S. Kim,^a James C.-M. Hsiao,^a Diana J. Lewis,^a Daniel I. Harjes,^{‡a} Christopher DiBiasio,^a Joseph L. Charest,^a and Jeffrey T. Borenstein^a

Received 00th January 20xx,
Accepted 00th January 20xx

DOI: 10.1039/x0xx00000x

Microfluidic lab-on-a-chip devices are changing the way that in vitro diagnostics and drug development are conducted, based on the increased precision, miniaturization and efficiency of these systems relative to prior methods. However, the full potential of microfluidics as a platform for therapeutic medical devices such as extracorporeal organ support has not been realized, in part due to limitations in the ability to scale current designs and fabrication techniques toward clinically relevant rates of blood flow. Here we report on a method for designing and fabricating microfluidic devices supporting blood flow rates per layer greater than 10 mL/min for respiratory support applications, leveraging advances in precision machining to generate fully three-dimensional physiologically-based branching microchannel networks. The ability of precision machining to create molds with rounded features and smoothly varying channel widths and depths distinguishes the geometry of the microchannel networks described here from all previous reports of microfluidic respiratory assist devices regarding the ability to mimic vascular blood flow patterns. These devices have been assembled and tested in the laboratory using whole bovine or porcine blood and in a porcine model to demonstrate efficient gas transfer, blood flow and pressure stability over periods of several hours. This new approach to fabricating and scaling microfluidic devices has the potential to address wide applications in critical care for end-stage organ failure and acute illnesses stemming from respiratory viral infections, traumatic injuries and sepsis.

Introduction

Devices and systems based on microfluidic design and construction are finding increased use in a wide range of applications in biological research and medicine[1]. These techniques have the potential to revolutionize chemical and biological analysis and clinical diagnostics, based on their ability to accelerate reaction rates, make more efficient use of precious reagents and patient samples, and increase the precision of critical processes. In the diagnostic space, microfluidic chips for early detection of viral infections, cancer and heart disease are becoming more prevalent[2]. On the therapeutics side, microfluidic technologies form the basis for most organ-on-chip platforms used for disease modelling and safety science currently under evaluation for broad adoption by the pharmaceuticals industry[3]. Over the course of the 30 year history of microfluidic technology development[4],[5],[6]. fabrication technologies and substrate materials have evolved in response to numerous factors

including ease and speed of prototyping, cost and increasing requirements for materials compatibility and biocompatibility[7].

In spite of great progress in lab-on-a-chip diagnostic and drug development platforms, the impact of microfluidics technologies on therapeutic medical devices has been limited, largely due to challenges in scaling the technology for various clinical applications where total flow rates and processing volumes can become quite large. One of the best examples of this domain is in the field of organ support technologies, such as kidney dialysis[8], [9] and respiratory assist devices, which are required to process hundreds of millilitres to litres per minute of whole blood in a circuit directly connected to the patient[10]. The precision of microfluidic devices at the cellular scale represents an attractive approach for augmenting or replacing current cartridge-based systems, which rely almost exclusively on flow blood through or around bundles of hollow fibres[11]. In the case of respiratory assist devices, an attractive feature of microfluidics is the ability to produce microchannels much closer in size to blood capillaries, and gas transfer membranes nearly as thin as the alveolar membrane in the human lung[12]. The reduction in microchannel diameter from the 250 micron size of most hollow fibres[13] to 25 – 50 micron range, and the ability to fabricate highly gas permeable membranes much thinner than the walls of hollow fibres, results in a greatly enhanced gas transfer efficiency for microfluidic oxygenators, as recently reported by several groups[12], [14]–[23],[24][25].

* Co-first authors

^a Bioengineering Division, Draper, Cambridge MA.

^b CRF Skirball Center for Innovation, Orangeburg, NY.

^c Thrombodyne, Salt Lake City UT.

[†] Current address: Brigham & Women's Hospital, Boston MA

[‡] Current address, Abbott Laboratories, Burlington MA

While increased gas transfer represents a very important technical advantage of microfluidic oxygenators, an even more critical parameter is the blood health as measured by indicators such as the propensity for thrombus formation and the generation of inflammatory markers in the blood during a procedure. For respiratory assist technologies such as Extracorporeal Membrane Oxygenation (ECMO) [26]–[28][29] and Extracorporeal Carbon Dioxide Removal (ECCO2R)[30][31]–[36], [37] and haemodialysis and hemofiltration procedures[38], [39], clinical implementation is severely hampered by complications such as clotting in the blood circuit, and therefore patients in a fragile hemodynamic state are often subjected to high levels of anticoagulant to prevent clot formation, which may lead to bleeding in the patient[10]. According to Virchow's Triad[40], these blood complications arise from three factors: (1) Blood contact with artificial surfaces along the device walls and tubing connections relative to the endothelialized surfaces in blood vessels, (2) Anomalous patterns of blood flow relative to the smooth flow found in physiological vasculature, and (3) Patient tendencies toward coagulopathies and other blood-related complications. Of these factors, the first two can be addressed by technology-based approaches, while the third remains a challenge associated with certain patient populations, trauma victims and many acute illnesses such as COVID-19[41],[42].

Scaling of microfluidic devices for blood-processing applications such as ECMO, ECCO2R and haemodialysis requires expansion and branching of microchannel networks in-plane and out-of-plane to enable higher volumes of blood flow consistent with clinical requirements. In order to recapitulate natural blood flow patterns in the microcirculation, microfluidic designs and fabrication techniques should follow physiologic design rules [43], and local geometries at branch points should be smoothly varying, with tapered and rounded features and symmetrical increases in the depth and width of blood vessels as joining flows are carried in or out of the small-diameter capillaries. Standard microchannel fabrication techniques utilizing photolithographic patterning [15] carry several significant limitations that hamper the ability to recapitulate physiological blood flow patterns. 1) Junctions between smaller and larger vessels realized by modulating photoresist thickness or etch time (even with isotropic etching) typically result in an abrupt rather than smoothly varying change in channel depth, a feature that is prone to clot formation[44] due to fluid shear gradients. 2) With conventional planar lithographic techniques utilizing one photoresist thickness or etch depth, channels increase in width but depth is fixed, leading to wide, shallow trunk lines that carry blood to the external device connections[45]. 3) Vertical manifolds joining stacked layers contain transitions with 90 degree angles where blood flows into the horizontal layer networks. All of these features lead to channel junctions that serve as a nidus for clot formation, precisely what the microfluidic designs set out to avoid.

Here we report on a new approach for fabrication of three-dimensional microchannel networks with smoothly varying cross-sections in both the horizontal and vertical dimensions. We invoke the use of precision machining with a Computer Numerical Control (CNC) machining tool, using settings and parameters capable of generating long, straight channels, joined at branch points with geometries that provide smooth, tapered features and symmetric changes in both the channel width and depth. A similar approach is used for the vertical vias that join stacks of horizontal layers, where the trunk lines carrying larger blood flows are smoothly varying in diameter, and the branch points are designed to have curved features that avoid sudden transitions in blood flow streamlines. For

the vertical distribution manifolds, we invoke direct machining of a transparent polymer structure produced in two halves that are then joined by thermal bonding. These manifolds are used to join multiple horizontal layers to form a stacked structure where blood is entrained in smoothly branching channel networks designed to avoid sudden transitions or shear gradients throughout the entire circuit. Microfluidic devices utilizing precision CNC machining have been previously reported for blood cleansing applications[46], but to our knowledge this is the first demonstration of horizontal and vertical microfluidic networks comprising smoothly varying channel depth and width throughout the entire circuit.

Computational modelling with finite element analysis tools was used to design microfluidic gas transfer devices, guided by simplified analytical relationships governing diffusion and permeation through PDMS films and blood. These analyses built upon the seminal work of Nair and Hellums [47], [48], Potkay[49] and Federspiel [30]. These devices were tested for blood oxygenation (ECMO) and carbon dioxide removal (ECCO2R) using whole bovine or porcine blood, and have been evaluated for gas transfer rates in single-layer and stacked (4-layer) configurations. A smaller device prototype, denoted RAD1, was tested for both oxygenation and carbon dioxide removal, and a larger device with longer channels, denoted RAD2, was used as a carbon dioxide removal device (ECCO2R configuration.)

In addition to

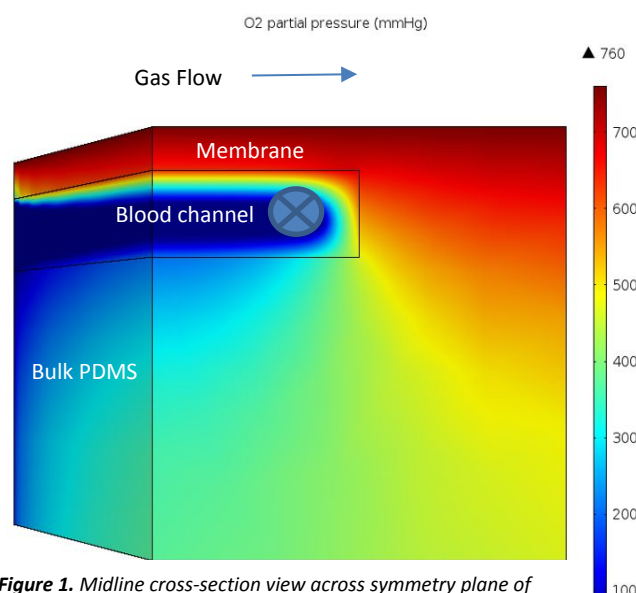


Figure 1. Midline cross-section view across symmetry plane of COMSOL model illustrating application of the simulation tool to predict oxygen partial pressure in the membrane, blood channel and bulk PDMS, according to the false color map at right. Blood flow direction is out of the page, orthogonal to gas flow.

laboratory evaluation of gas transfer, we report on hemocompatibility studies conducted using heparinized bovine or porcine blood in an external circuit, where platelet counts and pressure changes are monitored over time. Finally, as an initial proof-of-concept demonstration in large animals, we have evaluated the pressure stability of stacked microfluidic respiratory assist devices in extracorporeal circuits using a 40 kg swine model. These initial proof-of-concept studies demonstrate that highly stable performance of the blood circuit can be achieved over periods of several hours with relatively low levels of anticoagulant and no treatment of the device surfaces.

Experimental

Computational Approach for Modelling Shear and Flow

Computational fluid dynamic simulations were performed using COMSOL (COMSOL Inc., Burlington MA), using methods described previously [15]. Briefly, the COMSOL simulations were used to predict oxygen and carbon dioxide transfer as a function of geometric parameters including channel width, channel depth and membrane thickness, as well as operational parameters such as blood flow rate, haematocrit, and the starting concentration of blood gases in the venous input blood. Simulations were carried out on a simplified bilayer cross-section of an individual channel, using literature values for compositional properties such as the gas permeability of the PDMS membrane and walls. More complex mechanisms such as membrane distension due to forces imparted by the flowing blood were not accounted for in these models. In **Figure 1**, a COMSOL simulation illustrating the predicted spatial distribution of oxygen partial pressure is shown; this modelling approach was used to predict the influence of the most critical parameters such as membrane thickness and blood channel depth and length.

In addition the COMSOL modelling of oxygen and CO₂ transfer, fluid dynamic behaviour of the blood flow was also modelled, focusing on the blood distribution channels and the predicted velocity profiles at various locations within the gas transfer channels and the distribution manifolds. Simplifying assumptions similar to those described in Table 1 of the earlier reference [15] were applied, such as non-Newtonian rheology of the blood [50].

Device Design and Layout

We and others have previously reported microfluidic designs for respiratory assist devices, with most approaches invoking photolithographically produced master molds corresponding to a branching vascular network, opposing compartment for gas transfer, and intervening gas-permeable PDMS membrane [15][12], [17], [51], [52]. In virtually all of these cases, the photolithographically-defined masters comprised a single channel depth throughout the entire layer, with the larger entrance and exit blood distribution pathways dramatically widened to accommodate the larger flows without any increase in depth [25], a limitation that impelled our group to begin constructing multi-depth channel networks. In cases where multiple layers were joined, this was accomplished by fashioning vertical vias to carry blood from the cartridge inlet into the layer stack and then out again at the exit.

Here we invoke designs where each layer comprises a set of constant-depth parallel gas transfer channels joined at the inlet and outlet with manifolds that contain branching networks of smoothly varying width and depth larger distribution conduits. We report on two device designs, denoted as RAD1 and RAD2, that have been fabricated and tested for oxygen and carbon dioxide transfer in the laboratory. For the RAD1 device, multilayer stacks of 4 layers have been assembled and integrated with a manifold, and these devices have been evaluated for gas transfer and for proof-of-concept experiments in a large animal extracorporeal study.

The RAD1 vascular design comprises 112 channels of approximately 4.7 cm in length, while the RAD2 vascular design contains 176 channels of approximately 15.1 cm in length. Both device designs were constructed with two blood channel heights, 65 μm and 200 μm, to evaluate the trade off in hemocompatibility and gas transfer from these two channel heights. In each case, the oxygen compartment was designed to be aligned perpendicular to the vascular network such that alignment between layers was not critical. Key parameters for the designs are provided in **Supplementary Table I**. Layers were laid out using computer-aided

design software tool SolidWorks (Dassault Systèmes, Waltham, MA.) The blood distribution manifolds comprise a branching architecture curving off of the main trunk line, leading to two levels of bifurcations that then leads into the parallel gas transfer channels. The designs take advantage of the three-dimensional nature of the fabrication technology to permit varying depth conduits, an aspect that renders the manifold regions far more compact from a volume and surface area perspective than approaches where the channel depth is fixed throughout the network. In the SolidWorks-generated design, manifold conduits have a tapered bottom surface in a manner that avoids sudden changes in channel depth, a key feature that avoids one of the central source of flow disturbances in lithographically-defined microfluidic devices.

Device Fabrication

Both RAD1 and RAD2 devices consist of a blood/vascular layer and a gas layer sandwiching a gas transfer membrane. The layers for both RAD1 and RAD2 device designs were fabricated using similar methods.

Master Mold Fabrication

The blood vascular and gas layer microfluidic channel patterns were inverse machined into a block of aluminium to create a mold using a CNC milling machine (VU50A WITH FANUC 16i-M, Mitsui Seiki, Franklin Lakes, NJ). The molds were milled using a combination of diamond and ultra-fine finish end mills, carbide solid and diamond ball end mills and diamond rough end mills. After machining, all molds were cleaned with Acetone and Isopropyl Alcohol followed by 5 minutes in an ultrasonic bath. Surface roughness on the CNC-machined Al molds was measured to be less than 0.2 microns on average, generally superior to the level of roughness obtained using 3D printing technology, and particularly for very large area molds. A further advantage of CNC machining over 3D printing is the absence of leachable chemicals in the master mold, which might have a deleterious effect on blood health during device operation.

In order to facilitate ease of release of cast PDMS films, the molds were sputter coated using a KDF Sputterer (Rockleigh, New Jersey) with either 0.1 micron of Chromium or Titanium followed by 0.4 microns of Gold. The molds were then thiol coated by placing them face down in a bath of a 1mM solution of 1-Hexadecanethiol (Millipore Sigma, Burlington, MA) in Ethanol for a minimum of 2 hours.

Channel Layer Fabrication

A layer of Kapton® Polyimide plastic tape (7648A33, McMaster-Carr, Elmhurst, IL) was placed around the sides of the mold in order to create a barrier along the edge. Polydimethylsiloxane (PDMS) Med6015 (Nusil, Carpinteria, CA) was mixed at a ratio as prescribed by the manufacturer of 10 parts PDMS to 1 part curing agent. All mixing was performed in a speed mixer (FlackTek, Landrum, SC). For the RAD1 layers the smaller FlackTek DAC 150.1 FV mixer was used. For the RAD2 layers the larger FlackTek DAC 600.1 FVZ mixer was used in order to accommodate the larger volumes of PDMS required. After mixing, PDMS was poured into each mold and the molds with PDMS were placed in a vacuum desiccator for at least 45 minutes for RAD1 and 60 minutes for RAD2 in order to remove any trapped air. After degassing, the RAD1 layers were cured in an oven at 65C for at least 3 hours while RAD2 layers were cured at 150C for 45 minutes. Channel lengths were as indicated in the Results section, and channel widths for both RAD1 and RAD2 were 500 microns as designed. Spot check metrology measurements found channel widths of 475 – 517

microns, and the width is not a particularly sensitive parameter with regard to oxygen transfer efficiency or pressure drop.

Membrane fabrication

The membrane was fabricated by spin-coating a layer of PDMS on passivated silicon wafers. RAD1 membranes were spun on an 8 inch passivated silicon wafer using a CEE 100 spin coater (Brewer Science, Rolla, MO). Wafers were passivated by exposure to silane (trichlorosilane, Sigma-Aldrich, St. Louis MO) for at least 1 hour in a vacuum desiccator. The RAD2 membrane was spun on a 12 inch Polytetrafluoroethylene (PTFE) coated (GVD Corporation, Cambridge, MA) silicon wafer using a CEE 300 spin coater (Brewer Science, Rolla, MO). Each membrane thickness was controlled by rotation speed and time. The membrane thickness that was selected was fabricated by spinning at 1100 RPM for 60 seconds. The PDMS membrane thickness target was 50 microns, but the actual membrane thickness was measured as by Scanning Electron Microscopy at $46.5 \mu\text{m} \pm 0.9 \mu\text{m}$. The 50 micron target was selected because it was the thinnest membrane that could be handled with high yield during the microfabrication process. The 8 inch wafer membranes was cured in an oven at 65C for at least 90 minutes. The 12 inch wafer membrane was cured in an oven at 150C for 45 minutes.

Device Fabrication

The method for fabricating the RAD1 and RAD2 devices was similar other than the channel depth and pattern, and is described in the following. A schematic cross-section of a single-layer oxygenator with the blood channel layer bonded to the gas transfer membrane and then the oxygen channel layer is shown in **Figure 2a**. The membrane (purple film between the two channel regions) is targeted for a 50 micron thickness to achieve high rates of gas transfer while maintaining mechanical integrity during handling and operation.

Using an ink brayer, a thin layer of room temperature vulcanizing (RTV) silicone (DOWSIL™ 3140 RTV, Dow Corning, Midland, MI) was continually spread on a flat surface in order to form a uniform thickness of RTV. The brayer is then used to apply the thin film of RTV on to the gas layer. The gas layer was placed on the membrane that was still attached to the wafer. The wafer with the attached gas layer were cured in an oven at 65C for at least 8 hours. After curing, the gas layer with the attached membrane was removed from the wafer by first scoring the membrane along the edges of the gas layer. The gas layer with the attached membrane was carefully lifted off the wafer as not to tear the membrane.

Using the same brayer technique, as described above, a layer of RTV was applied to the blood vascular layer. The blood vascular layer was placed onto the membrane-gas layer stack such that the microfluidic vascular channels were perpendicular to the microfluidic gas channels. A visual alignment between layers was established using fiducial marks so that the overlaps and gaps between blood and oxygen channels and manifold regions would be consistent between devices. The combined two layer membrane device was placed in a 65C oven for a minimum of 4 hours to cure. Stainless steel tubing was inserted into the inlet and outlet ports of both the vascular and gas layers. A coating of PDMS was added around the edge of the entire device in order to ensure all edges were leak tight. PDMS was also used around the stainless steel tubing to ensure a leak tight connection between the tubing and the device. The devices were cured in an oven at 65C for 30 minutes. A four inch length of tubing (Masterflex Transfer Tubing, Tygon®, Cole-Parmer, Vernon Hills, IL) was slipped over all the inlet and outlet stainless steel tubes. A Luer

lock fitting (Masterflex Fitting, Polycarbonate, Straight, Cole-Parmer, Vernon Hills, IL) was attached to the opposite end of the Tygon® tube in order to allow for easy attachment to syringes and other tubing during testing.

Manifold Fabrication and Device Assembly

For multi-layer devices, layers are joined using a separate component at the inlet and outlet that utilizes the same design paradigm as the horizontal blood distribution manifold within each layer. This vertical manifold differs from existing multilayer microfluidic oxygenators [25], [53] in that the branching within the manifold occurs through a network of cylindrical channels of smoothly varying diameter designed to maintain constant shear rates for blood flow. These manifolds are constructed from direct-machined polycarbonate blocks as described below. For the stacked 4-layer RAD1 devices, the vertical manifold was 2.70 cm long by 1.91 cm wide by 0.63 cm in thickness, with an inlet trunk line branching four times into curved and tapered channels that interfaced with each blood inlet of the four layers in the RAD1 stack. An identical vertical manifold joins the outlets of each layer at the other side of the horizontal layers.

Multi-layer devices were fabricated by connecting the inlet and outlets of the vascular layers with these vertical manifolds. The blocks were fabricated in two halves. Each half was direct machined in a 3-Axis CNC milling machine using a variety of tooling including ball end mills. The two halves were thermocompression bonded together. Finally, the parts were vapour polished by Connecticut Plastics (Wallingford, CT) in order to remove all machining marks. A secondary machining operation was then performed in order to place the counter bores for the hypodermic tubing at the inlets and outlets. The hypodermic tubing was inserted into the block and affixed with UV cured epoxy (Dymax 1180-M-T-UR, Ellsworth Adhesives, Wilmington MA).

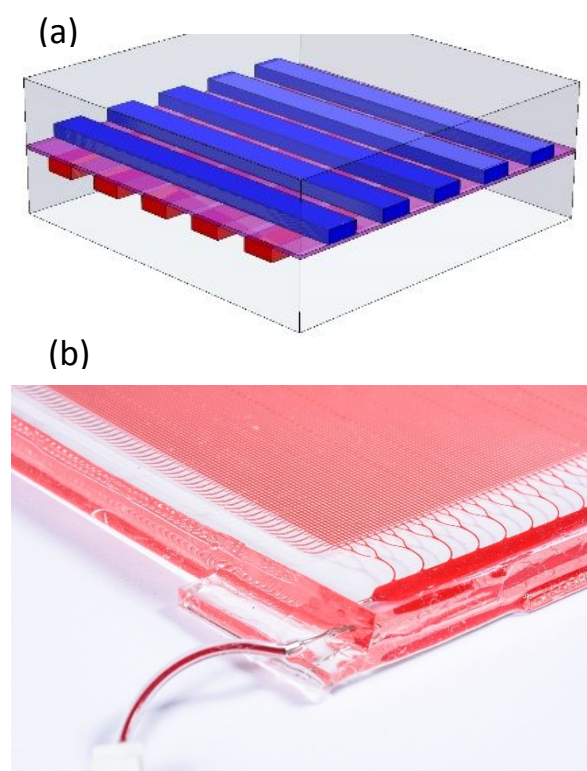


Figure 2. (a) Cross-section schematic of vascular/blood network layer, gas transfer membrane and oxygen network layer. The gas transfer membrane (purple region between the vascular and oxygen layers) is targeted for a 50 micron thickness. (b) Photograph of a section of RAD2 device illustrating the branching in-layer manifold leading to the blood channels, and the underlying perpendicular oxygen channel network on the other side of the gas transfer membrane.

Blood Testing

Benchtop testing

Bovine blood or porcine blood (LAMPPIRE Biological Laboratories, Inc., Pipersville, PA) was ordered to be delivered with Citrate Phosphate Dextrose (CPD) anticoagulant. Blood was placed into a 1 Liter transfer bag (Terumo BCT, Lakewood, CO) and heated in a water bath to 37C. After heating, the blood bag was transferred to a heated rocker (ThermoFisher, Waltham, MA) in order to maintain a temperature of 37C. The blood was pulled from the bag with a syringe and the syringe placed into a syringe pump (PHD Ultra, Harvard Apparatus, Holliston, MA) in order to control a constant blood flow rate. The Oxygen was sourced via a pressurized cylinder of Oxygen Grade 5.0 (99.999%) (Middlesex Gases & Technologies, Everett, MA). Gas flow rate was controlled with a mass flow controller (Alicat Scientific, Tucson, AZ). All connections were made with luer lock connectors. Outlet blood was analysed by hemoximeter (Avoximeter 4000, Instrumentation Laboratory, Bedford, MA) and a clinical blood gas analyser (GEM Premier 3000, Instrumentation Laboratory, Bedford, MA). These instruments were used to measure the O₂ and CO₂ content of blood as it entered and exited our device. For these experiments, blood was conditioned to venous conditions of 65% oxygen saturation and 45 mm Hg partial pressure of CO₂. When air was used as a transport gas a cylinder of Dry Grade Air (Middlesex Gases & Technologies, Everett, MA) was connected to the mass flow controller. Mass flow controller settings were adjusted for each gas entering the controller. Oxygen flow was passed through a CO₂ sensor (Qubit Systems, Kingston, Ontario, Canada) that was calibrated with a 2% carbogen gas mixture (Middlesex Gases & Technologies, Everett, MA). Oxygen and CO₂ transfer data was corrected to normalize for standard operating conditions including ambient pressure and temperature (760 mm Hg and 293 K), and for haematocrit levels (12 g/dL.) *In vitro* testing of pressure drop and platelet loss was conducted by monitoring pressure across the devices while flowing whole heparinized bovine blood through the devices for periods up to 2 hours. Thrombus formation was inferred by monitoring the reduction in circulating counts of radiolabelled (¹¹¹In) autologous platelets added to the blood flow during single pass studies.

Animal testing

Initial demonstration of the safety and operational stability of this device in a large animal model was performed using an anesthetized healthy Yorkshire swine (39±3 kg) model. A dual loop tubing configuration was set up to allow for a bypass loop that allows for independent control of the catheter flow and a device loop that can control the device flow rate. A 7 Fr Palindrome (Medtronic, Minneapolis, MN) heparinized catheter was placed into the jugular vein of each pig to allow central venous blood flow to the device. The bypass loop blood flow drew blood from the catheter with a peristaltic pump (520R, Watson Marlow, Falmouth, Cornwall, UK) at a maximum flow rate of 440 mL/min. The majority of the blood was returned to the animal through the catheter. The device loop also used a second peristaltic pump to draw blood, post the bypass pump, advancing it through the device and returning it to the bypass loop.

Three pressure sensors (Becton Dickinson DTX plus, Franklin Lakes, NJ) were placed in the loop one after the catheter, the second before the device and the third after the device. The pressure signals were connected to an amplifier (Gould Instruments, Chandler, AZ) where the signals were recorded and analysed with NOTOCORD-hem software (Le Pecq, France). All of the fluidic connections to the

device and placement of analysis equipment was similar to that previously described in the benchtop testing section above.

Hemocompatibility

Virchow's Triad identifies the governing factors controlling blood coagulation and thrombosis as 1) Blood flow patterns, 2) Blood-surface interactions, and 3) Patient coagulability. Our approach minimizes non-uniform flow and circulation zones by entraining the blood in a branching network similar to the human circulation and by avoiding sharp corners and sudden transitions by invoking a 3D microfabrication approach with precision machining. These techniques were implemented in both the photolithography created molds and the machined aluminium molds that were used in the fabrication of the device discussed throughout.

Data Analysis Techniques

The results of the CO₂ removal were reported in terms of the volume percent of CO₂ transferred from the blood to the sweep gas flowing through the gas transfer layer. This was calculated by taking the percent content of CO₂ read from the sensor on the gas outlet of the device, and calculating a flow rate of CO₂ into the sweep gas, in units of mL/min. The ratio of the flow rate of CO₂ to the blood flow rate in percent is the volume percent of CO₂ transfer. For oxygen transfer, blood gas analyzers were used to calculate the volume percent of oxygen transfer, where the oxygen concentration of the blood was multiplied by the blood flow rate to obtain the oxygen transfer rate in mL/min of oxygen. This was then converted to units of volume percent, as was done with CO₂ transfer.

Results and Discussion

Computational Analyses of Key Design Parameters

As described in the Experimental section, analytical equations based on literature reports [30], [48], [49] were generated and used to guide the designs. These analytical techniques were augmented by COMSOL modelling of oxygen and CO₂ transfer in representative single channel geometries. While these approaches serve as a useful guide for the design process, questions surrounding the effective gas permeability of PDMS, which is influenced by processing conditions [54], render these approaches subject to uncertainties in assignment of key model parameters. Further, the complexity of oxygen transport within the blood channel [48] and the multiple means by which CO₂ is carried in the blood [30] increase the challenge of precisely predicting gas transfer in these devices. For oxygen transport, modelling blood rheology and the various transport mechanisms through bulk PDMS, plasma and around haemoglobin binding sites, render this a complex task. For carbon dioxide, complications regarding transport via carbonic acid, haemoglobin (carbamates) and dissolved directly in the blood prevented model predictions for CO₂ transfer for specific device geometries from being made, but enabled analysis of the influence of various geometric and operational parameters on transfer rates. Quantitative predictions of volume percent oxygen transfer were possible, and these were applied to oxygenation studies of the RAD1 device, as described in the following.

Three-Dimensional Branching Microchannel Network

Single layer assembled RAD1 and RAD2 devices were cast at layer thicknesses of approximately 5 mm for each of the vascular and oxygen films, respectively, due to handling considerations. The gas transfer membranes in all devices were spin cast as described in the Methods section to a final thickness of 50 microns. Devices were

built with gas transfer channels either 65 or 200 microns in depth, as indicated in each specific case. Each of the RAD1 and RAD2 designs comprises a large array of parallel channels, 112 and 176, respectively. These channels are rectangular in geometry, and are joined at the edges of the layer by a branching in-layer manifold that is designed to distribute the blood evenly between channels. The in-layer manifold at the inlet enters at maximum width and becomes progressively narrower as it progresses toward the far end of the array. Branches curve off of the main channel at an angle and branch length designed to enable fully developed flow before blood reaches the next branch, finally forming two levels of bifurcations before reaching the linear array of gas transfer channels. The exit manifold is designed in a similar manner but with blood now flowing out through a widening pipe. COMSOL blood flow simulations are provided in a Supplementary File.

The abovementioned design features, describing the manner in which the blood flow patterns are spatially arranged in the x-y plane of the layer, could have been generated using photolithography rather than CNC machining of a master mold. The depth dimension, however, would be extremely difficult to vary using photolithographic techniques, since even grey-scale lithography[55], microfluidic masks[56] or multi-step photopatterning [57] processes would not be able to produce smoothly varying depths at transition regions. Other microfabrication approaches, such as laser ablation[58], xenon difluoride etching[59], electroplating[60] and solid freeform fabrication[61], have been reported as methods for producing multi-depth microchannel networks. While these promising approaches have resulted in functional microfluidic devices including endothelialized microvascular constructs, they are often limited by considerations such as surface roughness, limited geometric flexibility, and constraints on the maximum size of the master mold. Here we invoke CNC machining of metal master molds as a means to produce very large area inverse microchannel network patterns with smooth surfaces and wide flexibility in channel features. Smoothly varying channel depths ranging from the gas transfer channels (190 microns) to the deep connecting channel to the trunk line (344 microns) are shown in the SEM image of a PDMS vascular layer for the RAD2 design (Figure 3.)

The section shown in Figure 3 highlights the ability to smoothly and gradually vary the depth of channels as blood flows through the distribution manifold. In conventional photolithographically-based fabrication, the constant depth of the gas transfer channels (measured at 190 microns) would necessitate either branching into trunk lines limited to the same depth, or abrupt transitions into deeper regions where higher flow rates due to collection of a large number of channels exist. Here, we show a region with flow

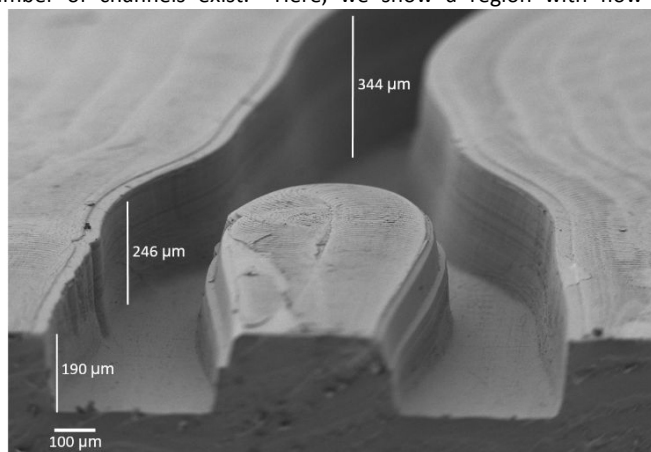


Figure 3. Scanning Electron Micrograph of a section of the in-layer manifold region of a PDMS vascular layer of a RAD2 device with a 200 micron blood channel depth. Note that the measured blood channel depth is 190 microns, increasing to 246 microns at the entry of the bifurcation and up to 344 microns in the deeper section of the channel. The floor of the channel smoothly varies along this transition region, and the sidewalls are very smooth, with occasional small ridges or grooves arising from the machining process.

collected from two 190 micron deep channels collected at a junction that smoothly varies in depth from the 190 micron transfer channels to the 344 micron depth of the collecting duct. The floor of these junction regions can be varied as smoothly and continuously as needed, due to the ability of the CNC machining to achieve such structures where photolithography techniques cannot.

Vertical Manifolds for Joining Multilayer Devices

Three-dimensional branches and bifurcations carry blood to the 112 parallel channels in a single RAD1 transfer layer, with rounded inlet and outlet ports connected to tubing during single transfer layer testing described in the Methods section. Here we report on testing of a stack of 4 RAD1 transfer layers connected in parallel using external vertical manifolds, each constructed as a half-plane with using direct machining as described in the Methods. Figure 4 shows a photograph of a 4-layer RAD1 stack with the vertical between-layer manifold shown in the foreground. This structure, which is direct-machined from polycarbonate, is formed in two halves that are designed using the same principles as the in-layer manifold. The halves are aligned and joined using thermal bonding as described in the Methods. Each half of the vertical manifold comprises semi-circular features, so that the complete manifold comprises a network of cylindrical channels with smoothly varying diameter from one channel dimension to the next. These vertical manifolds have bifurcating junctions rather than branching junctions, as shown in the image. Blood flows into the manifold through tubing that is inserted and glued to the inlet receptacle, and the manifold outlets are inserted via hypodermic needle segments and Silastic tubing into “mouse-hole” ports in the layer. While the details of the geometric approach to the manifold are not as critical for function of the device, the oxygen layers are interconnected in a similar manner.

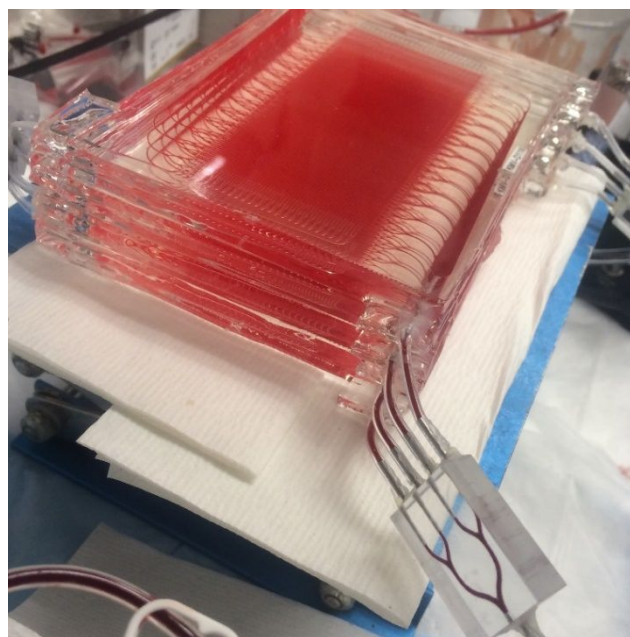


Figure 4. Photograph of 4-layer stacked RAD1 device filled with bovine blood and evaluated for oxygen and carbon dioxide blood gas transfer. Blood inlets and outlets are connected via vertical manifolds as shown at the lower right in the image (exit manifold is obscured by the stack, to the rear of the image.) Similar manifolds are used to connect the interspersed oxygen layers – at the lower left and upper right.

In Vitro Measurement of Gas Transfer – RAD1 Device

Oxygen and carbon dioxide removal rates were measured in vitro for single transfer layer and multilayer RAD1 devices using

techniques described in the Methods section. Briefly, citrate-phosphate-dextrose (CPD) anticoagulant was introduced into bovine blood collected and treated by a vendor and shipped overnight for use in laboratory testing the next day. Blood was conditioned to venous conditions as described earlier, and then flowed through the microfluidic oxygenator using a peristaltic pump at rates ranging from 0 – 40 mL/min (0 – 10 mL/min/layer for 4-layer devices.) Oxygenation was monitored by measuring the level of oxygen saturation and amount of dissolved oxygen in the blood as a function of blood flow rate, using a blood gas analyser and hemoximeter, as described in the Methods section. Carbon dioxide removal was monitored by measuring the CO₂ level in the headspace with an analyser, and experiments conducted across a range of blood flow rates and sweep gas flow rates. As described in the Methods, a sweep gas flow through the gas compartment is used to tune the rate of removal of CO₂ from the blood; higher sweep gas flows increase the amount of CO₂ removed.

The design described in the previous sections, known as RAD1, provided oxygen transfer levels of 5 volume percent, as defined in the Methods section, at blood flow rates in the 5 mL/minute per layer range. In **Figure 5a** oxygen transfer data is shown for three devices, each with 200 micron deep blood channels, tested on different days. Each device was tested between 3 and 7 times at each flow rate, and the average and standard deviations for each flow rate are displayed in the chart. Note that the performance between different devices and test days is relatively consistent across the low and high flow rates, but less consistent at mid-flow rates, and the devices provide a range of 3.3 - 6 volume percent oxygen transfer at 5 mL/min blood flow rate (average 4.87 volume percent) and 3.3 volume percent oxygen transfer at approximately 6.5 mL/min blood flow.

Variation between devices shown in **Figure 5a** (each combination of device/test day is plotted in a different marker color) stems from a number of sources, including build variability and changes in blood properties across different test days. Based on assessment of build variation and noting the range of blood properties (starting oxygen and CO₂ concentrations and haematocrit levels), we believe that the latter source is a more significant driver of variation. Generally, the channel width, length and depth varies only slightly between devices, since all devices are cast using the same master mold, and spot checking of dimensions shows only minor variations (+/- 3 – 5%) in these dimensions. A larger source of fabrication-based error arises from the changes in membrane thickness, as noted in the Methods section.

Figure 5b shows carbon dioxide removal as a function of blood flow rate for 4-layer RAD1 devices, along with error bars connoting standard error around the mean. Each device was tested for one 10-minute cycle, during the course of which 4 – 8 measurements of CO₂ concentration in the headspace were taken, as described in the Methods. After 10 minutes of blood flow and equilibration time for the CO₂ level measured by the analyser, CO₂ concentration was recorded and the volume percent calculated. As is seen in **Figure 5b**, RAD1 CO₂ removal was very consistent, with only RAD1-E showing an unusually high level of volume percent transfer over the course of the blood flow curve. The CO₂ removal volume percent (as defined in the Methods section) approached 10% at low flow rates. We observed that at blood flow rates of 2 mL/min/layer, or 8 mL/min for the 4-layer devices, volume percent transfer for carbon dioxide was in the range of 10 – 12%. For ECCO₂R treatments, typical

blood flows are in the range of 300 – 500 mL/min, while the rate of CO₂ removal ranges from 50 – 80 mL/min. The volume percent CO₂ removal is therefore closer to 20%, an efficiency that computational modelling has indicated will require longer gas transfer channels to increase the residence time in the device. Simply reducing flow rate in the RAD1 design would cause the flow velocities and concomitant wall shear stresses to drop to levels that may result in thrombus formation. Therefore, we designed and constructed a device with longer channels (RAD2) to target higher volume percent CO₂ removal, and blood flow rates similar to those utilized in haemodialysis treatments.

As described in the Methods, the RAD1 design was scaled to the

Multilayer RAD1 Device CO₂ and O₂ Transfer

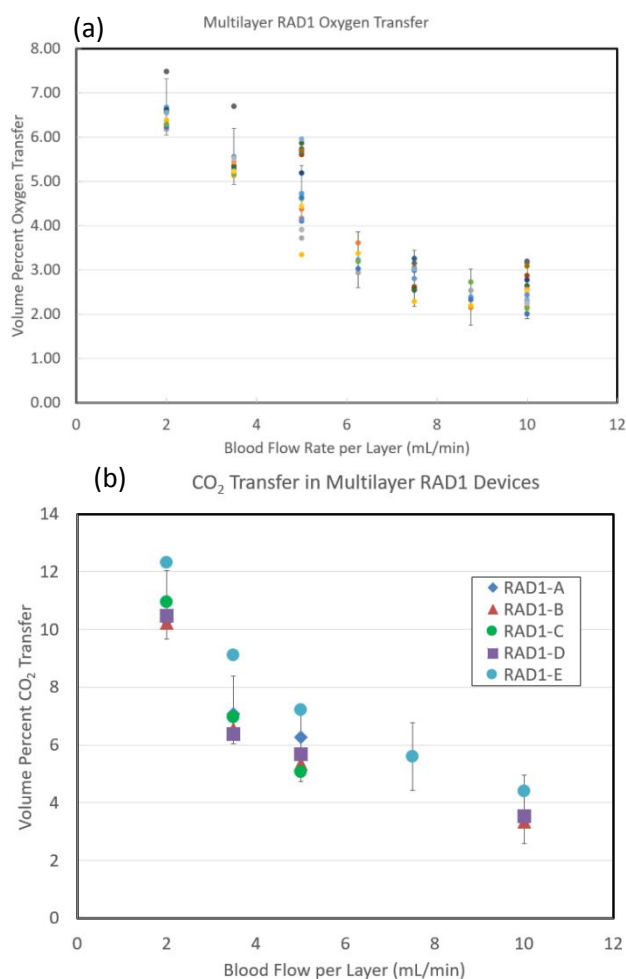


Figure 5. (a) Plot of three RAD1 devices showing volume percent oxygen transfer versus blood flow rate per layer in mL/min. Each device comprised a 4-layer stack joined by vertical manifolds. Each device was tested at each flow rate between 3 and 7 times, on separate days (color corresponds to a particular device tested in a particular day.) (b) Plot of five 4-layer RAD1 devices showing volume percent CO₂ removal versus blood flow rate per layer, with each device reporting one final volume percent transfer at the end of a 10-minute equilibration during blood flow. Error bars connote

RAD2 design, increasing the channel length from 4.7 to 15 cm and the number of channels from 112 to 176. The channel width in the parallel array for the RAD2 device was maintained at 500 microns.

The oxygen layer pattern was also designed with an orthogonal array of channels as in the RAD1 case. Two versions of the RAD2 device were designed and fabricated, one with a 65 μm channel depth (Figure 6) and the other with a channel depth of 200 μm . In each case, the in-layer manifold geometry followed the biomimetic 3D distribution paradigm described earlier, with a gradually narrowing trunk line and curving channels leading to the bifurcation regions.

In Vitro Measurement of Gas Transfer – RAD2 Device

The RAD2 design was tested in a single transfer layer format for CO_2 removal using the same procedures as were described for RAD1. These RAD2 devices were built with 65 micron deep channels, to further enhance CO_2 removal. In Figure 6, CO_2 removal in volume percent (calculated as mL/min CO_2 removed from the blood divided by mL/min blood flow) is plotted for each of 4 devices, with error bars connoting the standard deviation around the mean. For these devices, the 20 volume percent level is achieved for a single RAD2 layer at approximately 3 mL/min blood flow. For a 10 volume percent level of transfer, the flow rate for a single layer is 10 mL/min blood flow. The sweep gas flow rate used to obtain these results was 80 mL/min and the sweep gas was Grade 5.0 Oxygen. Tests were run across various sweep gas rates to explore the effect of sweep gas on carbon dioxide removal.

A high degree of consistency was seen between different devices and different test days / blood batches. The RAD2 exhibits a marked difference in performance from the RAD1, both by providing 10 volume percent CO_2 transfer at a much higher blood flow rate (10 mL/min versus 2 mL/min for a single layer), and by providing much higher volume percent transfer at low blood flow rates. It is this second characteristic, enabled by longer channels and longer residence times for the RAD2, that represents significant potential for future clinical impact, as described in the following analysis.

Initial evaluation of the RAD2 design indicates that the total number of device layers (n_l) necessary to achieve a given target level of CO_2 removal is significantly reduced by lengthening the blood channels in an individual device layer, as described in Equation (1). Where n_c denotes the number of channels and l_c represents the channel length. Eqn. (1) simply calculates the ratio of the product of the number of channels and the length of channels for the RAD2 over RAD1. This calculation yields a factor of 5.05, indicating that the number of layers (n_l) required to remove a targeted amount of CO_2 from the blood should drop by a factor of 5.05 when scaling from RAD1 to RAD2, simply by virtue of the increased lateral active area per layer.

$$\{n_c \times l_c (\text{RAD1})\} / \{n_c \times l_c (\text{RAD2})\} = 176 \times 15.1 \text{cm} / (112 \times 4.7 \text{cm}) = 5.05 \quad \{\text{Eqn. 1}\}$$

However, a more significant advantage of RAD2 over RAD1 is the ability to achieve volume percent CO_2 transfer of 20% or higher, as seen in Figure 6 as compared with Figure 5. The higher volume percent enables the device to function clinically at lower blood flow rates, for instance approaching the 400 mL/min typically administered during in-centre haemodialysis[8] for removal of 80 mL/min CO_2 . Equation (2) shows that when operating at 20 volume percent CO_2 transfer, the RAD2 device will require 133 layers to achieve 80 mL/min CO_2 removal at a blood flow rate of 400 mL/min. While this layer count is still quite high, a larger layer could cut this layer count by a factor of 2–3x, providing a path to clinical utilization

that would enable low-flow respiratory dialysis with a microfluidic ECCO2R device.

$$n_l = 0.20 \times v_p \times 400 \text{ mL/min} / (0.20 \times v_p \times 3 \text{ mL/min}) = 133 \quad \{\text{Eqn. 2}\}$$

In summary, the oxygen transfer efficiency of the RAD1 device, reaching and exceeding 5 volume % for blood flow rates of approximately 5 mL/minute, and CO_2 transfer efficiency of 15–25 volume % for the RAD2 at blood flow rates of 2–4 mL/min, are close to the targeted levels for clinical operation from an efficiency standpoint. The main challenge is then to scale these devices to blood flows sufficient for clinical operation.

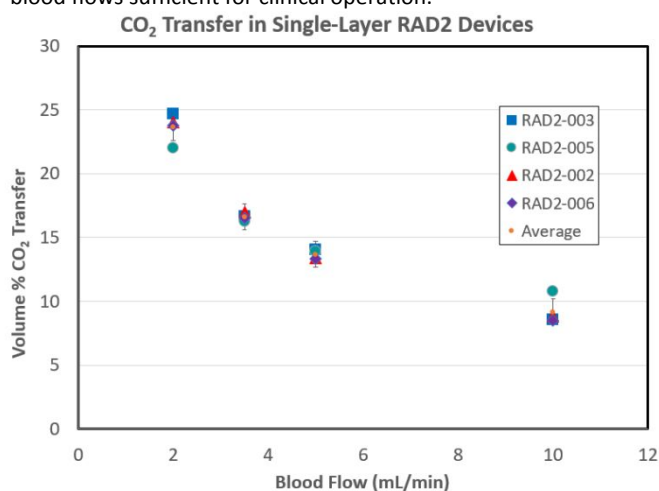


Figure 6. Plot of four RAD2 single layer devices showing volume percent carbon dioxide removal versus blood flow rate per layer in mL/min. Devices tested on different days with different batches of porcine blood. For each device, data reports one final volume percent transfer at the end of a 10-minute equilibration during blood flow. Error bars connote standard deviation around the average.

In Vitro Hemocompatibility – RAD1 Device

RAD1 single layer devices were evaluated in a laboratory setting for basic parameters of hemocompatibility, using freshly obtained bovine blood that has been anticoagulated to heparin concentrations of either 2.0 U/mL or 4.0 U/mL and introduced in a single-pass to a total of 4 devices. Sample pressure plots and platelet counts during testing for periods of 1 hour or more are shown in Figure 7a and 7b, respectively. In each plot, the measurement label corresponds the depth of the gas transfer channels in a RAD1 device, either 65 micron deep channels or 200 micron deep channels. In each case, the platelet counts in the blood remain relatively steady throughout the course of the test, indicating that platelet loss is minimal in this expedited model of device thrombosis[62], [63]. Pressure is seen to rise, and while the initial pressure is significantly higher in the shallow channel device as expected, the rate of pressure rise is similar between the two device depths. While the pressure rises significantly in only 2 h, in vitro configurations tend to exacerbate thrombus formation relative to extracorporeal tests, as described in the abovementioned references, and as is presented in the following section on our animal studies. Further, thrombus was noted primarily in and around the entry and exit tubing connectors in early prototypes, which guided design refinements. Future generations of devices will be designed and constructed to avoid the use of such coagulation-inducing materials in the circuit.

Extracorporeal Hemocompatibility – 4-Layer RAD1 Device

As described in the Methods, 4-layer RAD1 devices were also tested

in an extracorporeal circuit connected to an anesthetized 40 kg pig model. A schematic of the circuit used for the animal testing is shown in **Figure 8**. Three such independent procedures were completed, each lasting between 2 to 5 hours in duration, in order to evaluate the stability of the blood circuit over time. Following a baseline activated clotting time measurement (ACT), a heparin bolus (150–200 U/kg) was administered to achieve $ACT \geq 250$ s, after which blood was collected at a minimum of 30-minute intervals to measure and monitor ACT. Additional heparin boluses were administered to maintain $ACT > 250$ s, and no surface functionalization of devices was applied other than the use of a heparin-coated cannula, which was placed in the right internal jugular vein the swine. Since the maximum blood flow rate for the 4 layer device tested here was 40 mL/min, the device would not be of sufficient scale to provide necessary levels of oxygen or CO₂ removal, and therefore the pig was placed on a mechanical ventilator to provide respiratory function, with a focus on the maintenance of pressure and potential presence of clotting during the procedure. Pressures were monitored for each animal, showing a greater variation between animals at the start of the experiment than the changes that occurred during the test. These variations in initial blood pressure drop are akin to the differences in basal blood pressure levels between human patients.

As described in the Methods section, multiple pressure sensors were placed at targeted locations in the extracorporeal circuit, to detect whether the potential formation of thrombi might raise pressure, or in a more extreme case occlude microchannels over time. No observation of thrombi anywhere in the circuit was made at any point during the 5-hour experiments. Pressure measurements are shown in **Figure 9**. Here the systolic pressure is reported from three different animals and the average of all the data at each time point is shown in blue, demonstrating a remarkably stable performance over time, notwithstanding spurious spikes in the pressure sensors due to sensor instability or catheter manipulation. The pressure drops for each of the three animals varied fairly significantly, but the highest level of disparity was at the start of the experiment, suggesting that the differences were likely related more to the inherent blood pressure of each animal rather than the performance of each device. Specific sensors were taken offline at various points due to connection issues, but the signal marked in red on the chart shows that the pressure ended the 5.4 hour experiment virtually unchanged.

It is important to note that these initial animal experiments are principally focused on blood stability and not on device performance, as the scale of the devices is far too small to be useful in assessing gas transfer performance in an extracorporeal configuration. One of the principal concerns with microfluidic devices comprising arrays of shallow, narrow microchannels is that they may be prone to very rapid thrombus formation in an extracorporeal study, clogging the device and causing a catastrophic failure. Stable blood pressure drops, along with the absence of observation of significant clotting anywhere in the

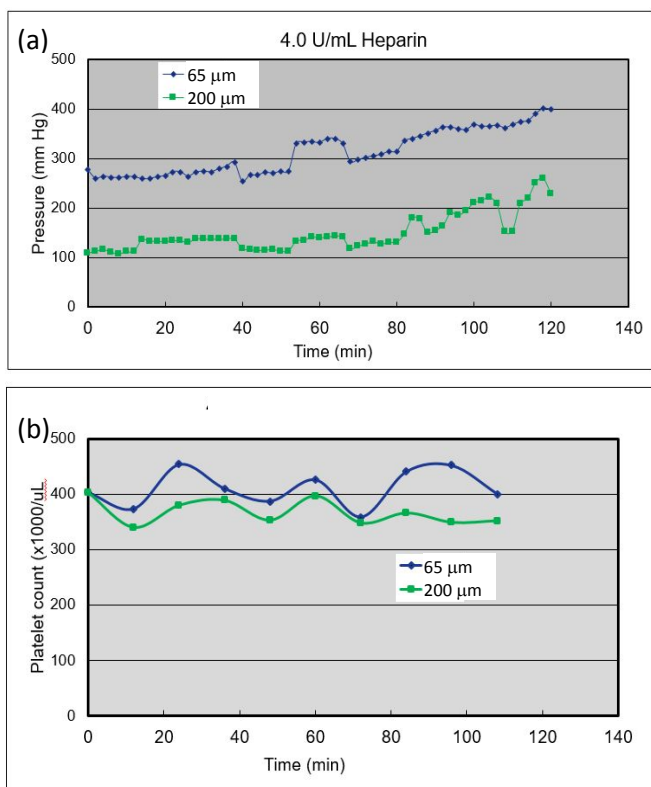
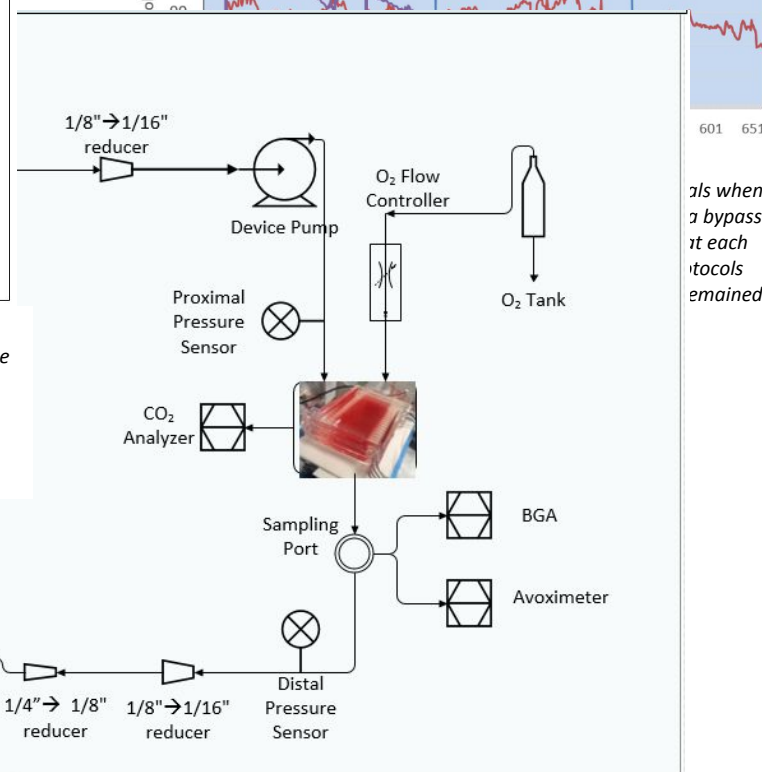
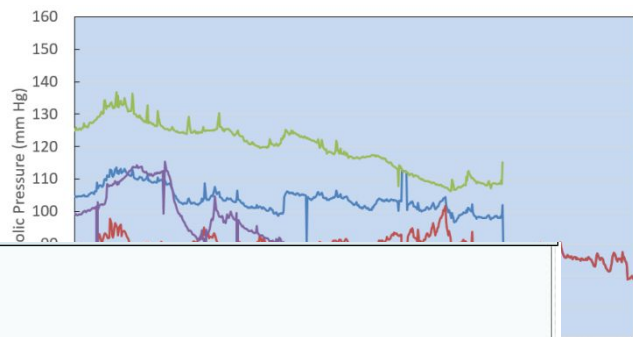


Figure 7. (a) Pressure plot for a 65-micron depth and 200-micron depth RAD1 device over a period of just under 2 hours, tested with flowing whole bovine blood heparinized to 4 U/mL. No circuit components were functionalized with any surface coatings. (b) Plot of platelet count in blood measured in the circuit as a function of time for the deep and shallow devices, showing no perceptible reduction during the experiment.



als when a bypass at each protocols remained

This jour

Figure 8. Circuit diagram for extracorporeal testing of RAD1 stacked ECO2R device with a 40 kg swine model. Note that a bypass loop was used to accommodate the 4-layer RAD1 stack, so that flow rates of 10–40 mL/min could be directed through the microfluidic device while flows of approximately 180 mL/min were drawn from the porcine vascular access, well within range of the design flow level of the catheter.

microfluidic device, represent encouraging signs that these devices can provide stable performance in an operational setting.

Conclusions

Here we demonstrate the application of high precision CNC machining as a means for producing branching networks that mimic key aspects of in vivo blood circulation. The ability to provide tapered and smoothly varying features at channel junctions and diameter changes represents one key advantage of this mold formation technology. A second key aspect is the ability to create 3-dimensional features for readily varying the channel depth along with channel width and length, a capability that becomes critical when smaller branches are joined to carry large flows in and out of a network. Here we demonstrate that capability along both the horizontal axis, where an in-layer manifold carries blood to a parallel array of over 100 microchannels, and in the vertical direction, where a precision-machined plastic feature distributes blood flow to a stack of 4 layers. While the microchannels retain the rectangular geometry seen in earlier reports of microfluidic oxygenators, a key difference in this report is the presence of smoothly varying depth branching channels and collecting ducts in both the horizontal and vertical distribution manifolds. These features enable the current devices to avoid the types of flow disturbances that occur when blood is subjected to a sudden change in channel depth as it traverses into and out of the gas transfer channels through the entry and exit manifolds. These scaling paradigms provide a pathway for future scaling to clinically translatable devices.

Gas transfer results show that the RAD1 design provides a 5 volume percent oxygen transfer at a blood flow rate of approximately 5 mL/min per layer. We evaluate 4-layer stacked RAD1 devices as a first demonstration of biomimetic branching distribution networks between layers of a respiratory assist device. Carbon dioxide removal from multilayer RAD1 devices is also examined, as a function of blood flow rate and at various sweep gas rates. We demonstrated CO₂ volume percent transfer of 10 – 12% at a blood flow rate of 2 mL/min per layer, in a non-optimized device, and CO₂ volume percent transfer greater than 20% at 3 mL/min in an optimized device with longer channels.

Hemocompatibility of the RAD1 design was evaluated in the laboratory and in initial extracorporeal testing with a large animal swine model. Platelet count and pressure rise in single-layer RAD1 devices was reported, with some thrombus noted in the entry and exit tubing regions. We tested 4-layer RAD1 devices in an extracorporeal circuit with an anesthetized 40 kg swine model, finding that standard heparinization protocols resulted in 5-hour stable function of the device in a circuit that flows 20 – 40 mL/min through the device. Challenges remain regarding optimization of gas transfer efficiency, reduction of pressure drop, automation of layer fabrication and manifold integration, steps necessary to minimize the size, cost and complexity of the ultimate device. Once these challenges are addressed, the technology presented here represents a promising new approach for advancing extracorporeal organ assist technologies toward wider, simpler and more reliable use for a range of critical care applications.

Author Contributions

J.A.S., A.A.G., J.L.C. and J.T.B. contributed to conceptualization of the work. J.G.T. and E.S.K. performed formal analysis of the computational design. A.A.G., J.G.T., D.A.L., J.C-M.H., C.D. and J.T.B. produced the device designs, J.C-M.H., A.A.G., D.I.H. and C.D. developed methodology for the device construction, and A.P. and S.P.S. developed methodology for extracorporeal and hemocompatibility testing, respectively. J.A.S., A.A.G., A.P., T.J.M., and A.M. performed benchtop experiments, S.P.S. conducted hemocompatibility testing, while J.A.S., A.A.G., A.P. and J.T.B. performed extracorporeal testing. D.J.L. performed device characterization, A.M. and J.T.B. conducted data curation. J.A.S., A.A.G., J.G.T., A.M. and J.T.B. performed data analysis. J.A.S., A.A.G. and J.T.B. wrote the original draft, and all authors contributed to the review and editing of the manuscript.

Conflicts of interest

The authors report no financial conflicts of interest with commercial entities associated with the technology reported in this work. Several of the authors (JAS, AAG, JGT, ESK, J.C.-M.H., D.I.H., C.D., J.L.C. and J.T.B.) are co-inventors on intellectual property related to the technology reported here, which is assigned to Draper.

Animal Experiments

The study was approved by the Institutional Animal Care and Use Committee and conducted in accordance with the Animal Welfare Act and the Guide for the Care and Use of Laboratory Animals (National Research Council, National Institutes of Health publication no. 85-23, revised 1996) at U.S. Department of Agriculture-licensed, Association for the Assessment and Accreditation of Laboratory Animal Care International-accredited animal research facility.

Acknowledgements

The authors gratefully acknowledge the support of Draper Laboratory and Johnson & Johnson toward the execution of this project. The U.S. Army Medical Research Acquisition Activity, 820 Chandler Street, Fort Detrick MD 21702-5014 is also an awarding and administering acquisition office. This work was supported in part by the U.S. Army, through the Peer Reviewed Medical Research Program under Award No W81XWH1910518. Opinions, interpretations, conclusions and recommendations are those of the author and are not necessarily endorsed by the U.S. Army. We would also like to acknowledge the contributions of Mark Laurenzi, Martin Nohilly and Catherine Owen of Johnson & Johnson, and Else Vedula, Brett Isenberg, Bryan Teece, Haleh Armian and David O'Dowd of Draper for technical and programmatic support.

References

- [1] D. R. Reyes *et al.*, "Accelerating Innovation and Commercialization Through Standardization of Microfluidic-Based Medical Devices," *Lab Chip*, 2020, doi: 10.1039/d0lc00963f.

- [2] F. Piraino, Š. Selimović, and K. K. Iniewski, *Diagnostic devices with microfluidics*. 2017.
- [3] L. A. Low and D. A. Tagle, "Tissue chips-innovative tools for drug development and disease modeling," *Lab on a Chip*. 2017, doi: 10.1039/c7lc00462a.
- [4] J. R. Anderson *et al.*, "Fabrication of topologically complex three-dimensional microfluidic systems in PDMS by rapid prototyping," *Anal. Chem.*, 2000, doi: 10.1021/ac9912294.
- [5] D. J. Beebe *et al.*, "Microfluidic tectonics: A comprehensive construction platform for microfluidic systems," *Proc. Natl. Acad. Sci. U. S. A.*, 2000, doi: 10.1073/pnas.250273097.
- [6] S. R. Quake and A. Scherer, "From micro- to nanofabrication with soft materials," *Science*. 2000, doi: 10.1126/science.290.5496.1536.
- [7] E. Berthier, E. W. K. Young, and D. Beebe, "Engineers are from PDMS-land, biologists are from polystyrenia," *Lab on a Chip*. 2012, doi: 10.1039/c2lc20982a.
- [8] C. R. Blagg, "The Early History of Dialysis for Chronic Renal Failure in the United States: A View From Seattle," *Am. J. Kidney Dis.*, 2007, doi: 10.1053/j.ajkd.2007.01.017.
- [9] J. Himmelfarb and T. A. Ikizler, "Medical progress: Hemodialysis," *N. Engl. J. Med.*, 2010, doi: 10.1056/NEJMr0902710.
- [10] W. Federspiel and K. Henchir, "Lung, Artificial: Basic Principles and Current Applications," in *Encyclopedia of Biomaterials and Biomedical Engineering, Second Edition - Four Volume Set*, 2008.
- [11] R. H. J. Hendrix, Y. M. Ganushchak, and P. W. Weerwind, "Contemporary Oxygenator Design: Shear Stress-Related Oxygen and Carbon Dioxide Transfer," *Artif. Organs*, 2018, doi: 10.1111/aor.13084.
- [12] J. A. Potkay, "The promise of microfluidic artificial lungs," *Lab on a Chip*. 2014, doi: 10.1039/c4lc00828f.
- [13] C. Ronco, A. Brendolan, C. Crepaldi, M. Rodighiero, and M. Scabardi, "Blood and dialysate flow distributions in hollow-fiber hemodialyzers analyzed by computerized helical scanning technique," *J. Am. Soc. Nephrol.*, 2001.
- [14] J. A. Potkay, M. Magnetta, A. Vinson, and B. Cmolik, "Bio-inspired, efficient, artificial lung employing air as the ventilating gas," *Lab Chip*, 2011, doi: 10.1039/c1lc20020h.
- [15] T. Kniazeva *et al.*, "Performance and scaling effects in a multilayer microfluidic extracorporeal lung oxygenation device," *Lab Chip*, vol. 12, no. 9, 2012, doi: 10.1039/c2lc21156d.
- [16] A. J. Thompson, L. H. Marks, M. J. Goudie, A. Rojas-Pena, H. Handa, and J. A. Potkay, "A small-scale, rolled-membrane microfluidic artificial lung designed towards future large area manufacturing," *Biomicrofluidics*, vol. 11, no. 2, 2017, doi: 10.1063/1.4979676.
- [17] K. A. Burgess, H. H. Hu, W. R. Wagner, and W. J. Federspiel, "Towards microfabricated biohybrid artificial lung modules for chronic respiratory support," *Biomed. Microdevices*, 2009, doi: 10.1007/s10544-008-9215-2.
- [18] W. I. Wu *et al.*, "Lung assist device: Development of microfluidic oxygenators for preterm infants with respiratory failure," *Lab Chip*, 2013, doi: 10.1039/c3lc41417e.
- [19] M. Dabaghi *et al.*, "An ultra-thin highly flexible microfluidic device for blood oxygenation," *Lab Chip*, 2018, doi: 10.1039/c8lc01083h.
- [20] D. M. Hoganson, H. I. Pryor, E. K. Bassett, I. D. Spool, and J. P. Vacanti, "Lung assist device technology with physiologic blood flow developed on a tissue engineered scaffold platform," *Lab Chip*, 2011, doi: 10.1039/c0lc00158a.
- [21] M. C. Kung, J. K. Lee, H. H. Kung, and L. F. Mockros, "Microchannel technologies for artificial lungs: (2) screen-filled wide rectangular channels," *ASAIO J.*, 2008, doi: 10.1097/MAT.0b013e31817ed9c8.
- [22] A. A. Gimbel, E. Flores, A. Koo, G. García-Cardeña, and J. T. Borenstein, "Development of a biomimetic microfluidic oxygen transfer device," *Lab Chip*, vol. 16, no. 17, 2016, doi: 10.1039/c6lc00641h.
- [23] T. Kniazeva, J. C. Hsiao, J. L. Charest, and J. T. Borenstein, "A microfluidic respiratory assist device with high gas permeance for artificial lung applications," *Biomed. Microdevices*, vol. 13, no. 2, 2011, doi: 10.1007/s10544-010-9495-1.
- [24] J. D. H. T.C. Page, W. R. Light, "Oxygen transport in 10 microns artificial capillaries," in *Oxygen Transport to Tissue XXI*, 1999.
- [25] A. A. Gimbel *et al.*, "A High Gas Transfer Efficiency Microfluidic Oxygenator for Extracorporeal Respiratory Assist Applications in Critical Care Medicine," *Artif. Organs*, 2021, doi: 10.1111/aor.13935.
- [26] D. Palanzo, F. Qiu, L. Baer, J. B. Clark, J. L. Myers, and A. Ündar, "Evolution of the extracorporeal life support circuitry," *Artificial Organs*. 2010, doi: 10.1111/j.1525-1594.2010.01127.x.
- [27] M. Schoberer *et al.*, "Fifty Years of Work on the Artificial Placenta: Milestones in the History of Extracorporeal Support of the Premature Newborn," *Artificial Organs*. 2012, doi: 10.1111/j.1525-1594.2011.01404.x.
- [28] B. W. Gray, J. W. Haft, J. C. Hirsch, G. M. Annich, R. B. Hirschl, and R. H. Bartlett, "Extracorporeal life support: Experience with 2,000 patients," *ASAIO Journal*. 2015, doi: 10.1097/MAT.0000000000000150.
- [29] D. Brodie and M. Bacchetta, "Extracorporeal membrane oxygenation for ARDS in adults," *N. Engl. J. Med.*, 2011, doi: 10.1056/NEJMc1103720.
- [30] L. W. Lund and W. J. Federspiel, "Removing extra CO₂ in COPD patients," *Curr. Respir. Care Rep.*, 2013, doi: 10.1007/s13665-013-0057-x.
- [31] B. Y. Chang and S. P. Keller, "Dual Carbon Dioxide Capture to Achieve Highly Efficient Ultra-Low Blood Flow Extracorporeal Carbon Dioxide Removal," *Ann. Biomed. Eng.*, 2020, doi: 10.1007/s10439-020-02477-1.
- [32] R. G. Jeffries *et al.*, "Pre-clinical evaluation of an adult extracorporeal carbon dioxide removal system with active mixing for pediatric respiratory support," *Int. J. Artif. Organs*, 2014, doi: 10.5301/ijao.5000372.
- [33] M. Fitzgerald *et al.*, "Extracorporeal carbon dioxide removal for patients with acute respiratory failure secondary to the acute respiratory distress syndrome: A systematic review," *Critical Care*. 2014, doi:

- 10.1186/cc13875.
- [34] D. Brodie, A. S. Slutsky, and A. Combes, "Extracorporeal life support for adults with respiratory failure and related indications: A review," *JAMA - J. Am. Med. Assoc.*, 2019, doi: 10.1001/jama.2019.9302.
- [35] V. Fanelli *et al.*, "Feasibility and safety of low-flow extracorporeal carbon dioxide removal to facilitate ultra-protective ventilation in patients with moderate acute respiratory distress syndrome," *Crit. Care*, 2016, doi: 10.1186/s13054-016-1211-y.
- [36] J. Allardet-Servent, M. Castanier, T. Signouret, R. Soundaraveolu, A. Lepidi, and J. M. Seghboyan, "Safety and efficacy of combined extracorporeal CO₂ removal and renal replacement therapy in patients with acute respiratory distress syndrome and acute kidney injury: The pulmonary and renal support in acute respiratory distress syndrome study," *Crit. Care Med.*, 2015, doi: 10.1097/CCM.0000000000001296.
- [37] M. E. Cove, G. MacLaren, W. J. Federspiel, and J. A. Kellum, "Bench to bedside review: Extracorporeal carbon dioxide removal, past present and future," *Critical Care*. 2012, doi: 10.1186/cc11356.
- [38] D. Tharmaraj and P. G. Kerr, "Haemolysis in haemodialysis," *Nephrology*. 2017, doi: 10.1111/nep.13119.
- [39] J. H. M. Smits, J. Van Der Linden, P. J. Blankestijn, and T. J. Rabelink, "Coagulation and haemodialysis access thrombosis," *Nephrol. Dial. Transplant.*, 2000, doi: 10.1093/ndt/15.11.1755.
- [40] T. Watson, E. Shantsila, and G. Y. Lip, "Mechanisms of thrombogenesis in atrial fibrillation: Virchow's triad revisited," *The Lancet*. 2009, doi: 10.1016/S0140-6736(09)60040-4.
- [41] G. J. Peek *et al.*, "Efficacy and economic assessment of conventional ventilatory support versus extracorporeal membrane oxygenation for severe adult respiratory failure (CESAR): a multicentre randomised controlled trial," *Lancet*, 2009, doi: 10.1016/S0140-6736(09)61069-2.
- [42] G. Tavazzi *et al.*, "Myocardial localization of coronavirus in COVID-19 cardiogenic shock," *Eur. J. Heart Fail.*, 2020, doi: 10.1002/ejhf.1828.
- [43] C. D. Murray, "The Physiological Principle of Minimum Work: I. The Vascular System and the Cost of Blood Volume," *Proc. Natl. Acad. Sci.*, 1926, doi: 10.1073/pnas.12.3.207.
- [44] M. K. Runyon, C. J. Kastrop, B. L. Johnson-Kerner, T. G. Van Ha, and R. F. Ismagilov, "Effects of shear rate on propagation of blood clotting determined using microfluidics and numerical simulations," *J. Am. Chem. Soc.*, 2008, doi: 10.1021/ja076301r.
- [45] D. R. Emerson, K. Cieřlicki, X. Gu, and R. W. Barber, "Biomimetic design of microfluidic manifolds based on a generalised Murray's law," *Lab Chip*, 2006, doi: 10.1039/b516975e.
- [46] J. H. Kang *et al.*, "An extracorporeal blood-cleansing device for sepsis therapy," *Nat. Med.*, vol. 20, no. 10, pp. 1211–1216, 2014, doi: 10.1038/nm.3640.
- [47] P. K. Nair, J. D. Hellums, and J. S. Olson, "Prediction of oxygen transport rates in blood flowing in large capillaries," *Microvasc. Res.*, 1989, doi: 10.1016/0026-2862(89)90005-8.
- [48] P. K. Nair, N. S. Huang, J. D. Hellums, and J. S. Olson, "A simple model for prediction of oxygen transport rates by flowing blood in large capillaries," *Microvasc. Res.*, 1990, doi: 10.1016/0026-2862(90)90070-8.
- [49] J. A. Potkay, "A simple, closed-form, mathematical model for gas exchange in microchannel artificial lungs," *Biomed. Microdevices*, 2013, doi: 10.1007/s10544-013-9736-1.
- [50] S. S. Shibeshi and W. E. Collins, "The rheology of blood flow in a branched arterial system," *Appl. Rheol.*, 2005, doi: 10.1515/arh-2005-0020.
- [51] E. K. Bassett, D. M. Hoganson, J. H. Lo, E. J. N. Penson, and J. P. Vacanti, "Influence of vascular network design on gas transfer in lung assist device technology," *ASAIO J.*, 2011, doi: 10.1097/MAT.0b013e318234a3ac.
- [52] N. Rochow *et al.*, "An integrated array of microfluidic oxygenators as a neonatal lung assist device: In vitro characterization and in vivo demonstration," *Artif. Organs*, 2014, doi: 10.1111/aor.12269.
- [53] M. Dabaghi *et al.*, "A Pumpless Microfluidic Neonatal Lung Assist Device for Support of Preterm Neonates in Respiratory Distress.," *Adv. Sci. (Weinheim, Baden-Wurttemberg, Ger.)*, vol. 7, no. 21, p. 2001860, Nov. 2020, doi: 10.1002/adv.202001860.
- [54] D. A. Markov, E. M. Lillie, S. P. Garbett, and L. J. McCawley, "Variation in diffusion of gases through PDMS due to plasma surface treatment and storage conditions," *Biomed. Microdevices*, 2014, doi: 10.1007/s10544-013-9808-2.
- [55] Y. Nam, M. Kim, and T. Kim, "Fabricating a multi-level barrier-integrated microfluidic device using grey-scale photolithography," *J. Micromechanics Microengineering*, 2013, doi: 10.1088/0960-1317/23/10/105015.
- [56] C. Chen, D. Hirdes, and A. Folch, "Gray-scale photolithography using microfluidic photomasks," *Proc. Natl. Acad. Sci. U. S. A.*, 2003, doi: 10.1073/pnas.0435755100.
- [57] K. Brower, A. K. White, and P. M. Fordyce, "Multi-step variable height photolithography for valved multilayer microfluidic devices," *J. Vis. Exp.*, 2017, doi: 10.3791/55276.
- [58] D. H. Kam, L. Shah, and J. Mazumder, "Femtosecond laser machining of multi-depth microchannel networks onto silicon," *J. Micromechanics Microengineering*, 2011, doi: 10.1088/0960-1317/21/4/045027.
- [59] J. P. Camp, T. Stokol, and M. L. Shuler, "Fabrication of a multiple-diameter branched network of microvascular channels with semi-circular cross-sections using xenon difluoride etching," *Biomed. Microdevices*, 2008, doi: 10.1007/s10544-007-9123-x.
- [60] J. T. Borenstein *et al.*, "Functional endothelialized microvascular networks with circular cross-sections in a tissue culture substrate," *Biomed. Microdevices*, vol. 12, no. 1, 2010, doi: 10.1007/s10544-009-9361-1.

- [61] M. G. A. Mohamed, H. Kumar, Z. Wang, N. Martin, B. Mills, and K. Kim, "Rapid and inexpensive fabrication of multi-depth microfluidic device using high-resolution LCD stereolithographic 3D printing," *J. Manuf. Mater. Process.*, 2019, doi: 10.3390/jmmp3010026.
- [62] Z. Zhang, J. Borenstein, L. Guiney, R. Miller, S. Sukavaneshvar, and C. Loose, "Polybetaine modification of PDMS microfluidic devices to resist thrombus formation in whole blood.," *Lab Chip*, vol. 13, no. 10, pp. 1963–1968, May 2013, doi: 10.1039/c3lc50302j.
- [63] S. Sukavaneshvar, "Device thrombosis and pre-clinical blood flow models for assessing antithrombogenic efficacy of drug-device combinations.," *Adv. Drug Deliv. Rev.*, vol. 112, pp. 24–34, Mar. 2017, doi: 10.1016/j.addr.2016.07.009.